CrossMark

RESEARCH ARTICLE

The influence of the stagnation zone on the fluid dynamics at the nozzle exit of a confined and submerged impinging jet

Nicholas Jeffers[1] · Jason Stafford[1] · Ciaran Conway[2] · Jeff Punch[2] · Edmond Walsh[3]

Abstract Low profile impinging jets provide a means to achieve high heat transfer coefficients while occupying a small quantity of space. Consequently, they are found in many engineering applications such as electronics cooling, annealing of metals, food processing, and others. This paper investigates the influence of the stagnation zone fluid dynamics on the nozzle exit flow condition of a low profile, submerged, and confined impinging water jet. The jet was geometrically constrained to a round, 16-mm diameter, square-edged nozzle at a jet exit to target surface spacing (H/D) that varied between $0.25 < H/D < 8.75$. The influence of turbulent flow regimes is the main focus of this paper; however, laminar flow data are also presented between $1350 < Re < 17,300$. A custom measurement facility was designed and commissioned to utilise particle image velocimetry in order to quantitatively measure the fluid dynamics both before and after the jet exits its nozzle. The velocity profiles are normalised with the mean velocity across the nozzle exit, and turbulence statistics are also presented. The primary objective of this paper is to present accurate flow profiles across the nozzle exit of an impinging jet confined to a low H/D, with a view to guide the boundary conditions chosen for numerical simulations confined to similar constraints. The results revealed in this paper suggest that the fluid dynamics in the stagnation zone strongly influences the nozzle exit velocity profile at confinement heights between $0 < H/D < 1$. This is of particular relevance with regard to the choice of inlet boundary conditions in numerical models, and it was found that it is necessary to model a jet tube length $L/D > 0.5$—where D is the inner diameter of the jet—in order to minimise modelling uncertainty.

1 Introduction

Impinging jets are applied to a wide range of engineering applications including the annealing of metals and plastics, turbine blade cooling, food processing, and more recently, electronics cooling. This paper focuses on the nozzle exit velocity profile of an impinging jet confined to a low nozzle-to-plate spacing (H/D). There have been a number of reviews identifying the significant parameters that impact the fluid dynamics of an impinging jet—(Webb and Ma 1995; Lienhard 1995; Martin et al. 1977; Jambunathan et al. 1992; Polat et al. 1989; Garimella and Rice 1995). These fundamental parameters include: nozzle-to-plate spacing (H/D), Reynolds number (Re), nozzle diameter, nozzle cross-sectional geometry, nozzle length-to-diameter (L/D), flow confinement, and inlet turbulence level. Changing any one of these parameters can influence the fluid dynamics at the nozzle exit of the impinging jet. The aim of this paper is to present accurate nozzle exit flow profiles of an impinging jet confined to a low H/D to inform the boundary conditions selected in numerical simulations confined to similar constraints.

The features of an impinging jet can be divided into three distinctly different zones: the free jet zone; the stagnation zone; and the wall jet zone, as shown in Fig. 1.

✉ Nicholas Jeffers
  nick.jeffers@alcatel-lucent.com

1 Bell Labs, Thermal Management Research Group, Alcatel-Lucent, Dublin, Ireland

2 Connect, Stokes Institute, University of Limerick, Limerick, Ireland

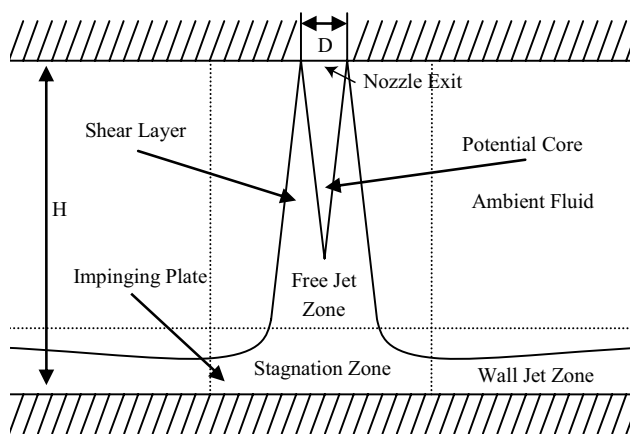3 Osney Thermo-Fluids Laboratory, University of Oxford, Oxford, United Kingdom

Fig. 1 Impinging jet schematic illustrating the free jet zone, the stagnation zone, and the wall jet zone

– The free jet zone refers to the region where the jet is unaffected by the impingement surface Deshpande and Vaishnav (1982). The free jet zone comprises a potential core surrounded by a shear layer. Within the potential core of the jet, both the fluid velocity and turbulence intensity remain unaffected by the shear layer. The shear layer entrains the ambient fluid creating high levels of turbulence that, in turn, cause both the radial spread of the jet and the core diameter to diminish. When the shear layer penetrates the centre-line of the potential core, its axial velocity begins to decrease and the turbulence intensity begins to increase. Beyond the potential core of the jet, a decrease in centre-line velocity is seen coupled to an increase in turbulence.

– The stagnation zone is created when a jet impinges onto a target surface. Within the stagnation zone, the axial velocity of the jet decelerates and is deflected in the radial direction. This zone initiates at the onset of the deceleration of axial velocity, which is caused by the impingement on the target surface. Martin et al. (1977) and Gardon and Akfirat (1965) showed that the jet development begins to be influenced by the target surface at approximately $H/D = 1.2$ above the impinging surface. Fitzgerald and Garimella (1998) also showed that for $H/D < 1.5$, the centre-line velocity drops rapidly as a result of the stagnation zone of the impinging jet.

– The wall jet zone exists beyond the radial limits of the stagnation zone, where the jet develops radially across the target surface. While complex fluid dynamics occur in this region, as shown by Jeffers (2009), it is beyond the focus of this paper, which is concerned with the fluid dynamics across the jet's nozzle exit.

The velocity profile across the nozzle exit is generally a predefined boundary condition in the majority of numerical simulations found in the literature. This technique is used to simplify the model in order to save on computational time, especially if the model includes complex impingement features and arrays of jets. For convenience, the majority of these simulations employ either a fully developed or undeveloped flat nozzle exit velocity profile as an inlet boundary condition. The ultimate precision of any numerical simulation relies on the accuracy of these predefined boundary conditions. Hadziabdic and Hanjalic (2008) compiled a large eddy simulation (LES) to model the fluid dynamics and heat transfer from a round jet impinging on a flat plate held at $H/D = 2$. They also generated a separate LES simulation to produce a fully developed turbulent pipe flow, from which they extracted the fluid dynamics at every time step to replicate the nozzle exit condition of a fully developed turbulent impinging jet. Alimohammadi et al. (2014) separately modelled a long nozzle pipe and mapped the nozzle exit to the domain inlet to save on computational time. Hattori and Nagano (2004) also used a fully developed turbulent pipe flow to define the flow condition at the nozzle exit. Their primary objective was to model an impinging jet using direct numerical simulation (DNS) and examine the effects of H/D spacings between $0.5 < H/D < 2.0$. Behnia et al. (1999) also employed a fully developed turbulent flow profile for their nozzle inlet condition and performed a numerical analysis to determine the effects of jet confinement coupled with the influence of H/D ratios between $0.25 < H/D < 2$. Satake and Kunugi (1998) performed a DNS simulation for an impinging jet confined to a $H/D = 6$. They assumed that the velocity profile at the nozzle exit was fully developed and turbulent. Caggese et al. (2013) modelled an entire plenum section in order to avoid inaccuracies in their numerical results, this approach computationally intensive. Thielen et al. (2005) compiled numerical simulations using $k - \varepsilon$ and v^2f methods to model impinging jet arrays confined to a $H/D = 4$ and utilised an undeveloped flat velocity profile across the nozzle exit. There are three physical parameters which influence the velocity profile at the nozzle exit: nozzle diameter to jet tube length (L/D) aspect ratio; the nozzle shape, and the fluid dynamics associated with the stagnation zone when the jet is confined to low H/D ratios.

This paper considers the influence of the stagnation zone on the velocity profile at the nozzle exit for low H/D confinements. There is literature that supports the notion that the fluid dynamics of the impinging jet change as the H/D ratio is reduced; however, the data presented are very limited. Fitzgerald and Garimella (1998) showed that for $H/D > 1.5$, the centre-line velocity of the jet was unaffected by the impinging plate; however, for $H/D < 1.5$, the

centre-line velocity of the jet drops rapidly. These results agree with those found by Martin et al. (1977) and Gardon and Akfirat (1965) who reported that the target surface begins to have an effect at 1.2 D. This paper presents an in-depth analysis of the nozzle exit flow conditions of impinging jets affected by its stagnation zone. The results from this study are of particular relevance for contemporary numerical simulations, where the nozzle exit condition is usually a predefined boundary condition to save on computational time. A submerged and confined water jet was experimentally assessed for Reynolds numbers between $1350 < Re < 17{,}300$, and confinement heights between $0.25 < H/D < 8.75$. The main focus of this paper is towards turbulent jet flow regime; however, laminar flow data are also presented. Particle image velocimetry (PIV) was used to quantitatively measure the flow fields surrounding the nozzle exit. The results presented show that the fluid dynamics in the stagnation zone of an impinging jet affect the nozzle exit velocity profile for confinement heights between $0.25 < H/D < 1$. It was shown that as the H/D ratio decreases from $H/D = 1$, the stagnation zone backpressure effect increases. To support what was found experimentally, numerical simulations of a turbulent jet impingement were also conducted using the Reynolds-averaged Navier–Stokes (RANS) approach. These models were used to predict the flow features generated as a result of the stagnation zone backpressure phenomena. A parametric study, using this numerical approach, was also conducted. The main objective of this paper is to investigate the influence of the initial boundary conditions, assumed at the nozzle exit, on the predicted velocity fields above the impingement surface in numerical models. The resultant findings from this paper can be used for clearly defining, and therefore reducing uncertainty, in the nozzle boundary condition when simulating low H/D jet impingement scenarios (i.e. $H/D < 1$).

2 Experimental and CFD methods

The objective of this study is to evaluate the effects of the stagnation zone fluid dynamics on the nozzle exit velocity profile of an impinging jet confined to low H/D ratios. In order to achieve this objective, a custom measurement facility was created for experimental assessments, and a numerical model was developed to replicate this test facility. The experimental facility was capable of performing PIV, which was used to generate time-averaged velocity magnitude plots. PIV was chosen as it is a non-invasive method of achieving instantaneous 2D velocity vector field measurements. From these plots, the flow fields surrounding the stagnation zone of the jet were established. The experimental results were validated against theoretical velocity profile predictions. The experimental apparatus, test procedure, numerical analysis and uncertainty analysis are presented in this section.

2.1 Experimentation

Velocity field measurements were taken using PIV on a confined and submerged water jet over a range of H/D ratios between $0.25 < H/D < 8.75$ to fully characterise the effect of this backpressure phenomenon surrounding the stagnation zone. Figure 2 shows the experimental apparatus used to visualise the fluid dynamics of a water jet. The jet in this facility exits a transparent straight round pipe with an inner diameter $D = 16$ mm, outer
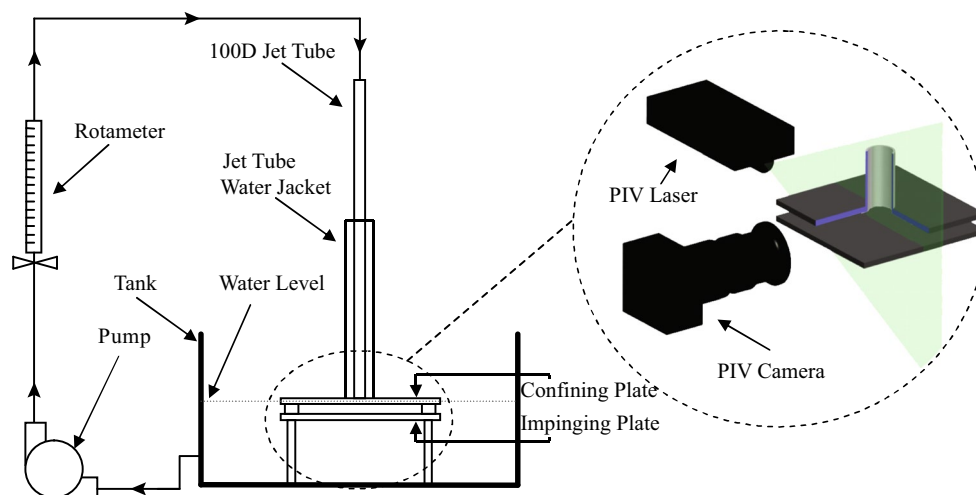

Fig. 2 PIV experimental apparatus

Table 1 PIV parameters

PIV parameters	$H/D = 0.25$	$H/D = 0.37$	$H/D = 0.62$	$H/D = 1$	$H/D = 8.75$	Units
Length per pixel	10.71	14.46	14.56	17.46	17.24	μm
Vector spacing	208	180	235	200	178	μm
Initial interrogation size	40×40					–
Final interrogation size	24×24					–
Time between images	10–200					μs
Laser sheet thickness	1.2					mm
Tracer particle size	8–12					μm
Camera resolution	1600×1200					Pixel

diameter 20 mm, and a length of 1600 mm that equates to 100 diameters (D). The tube length was chosen to insure that the flow was fully developed by the nozzle exit. Bejan (2004a, b) presented two equations, which showed for the range of Reynolds numbers (Re) tested in this paper, that fully developed laminar and turbulent pipe flow occurs at approximately 100 and 10 D, respectively. Fox et al. (2004a) reported that a turbulent pipe flow may not be fully developed after an entrance length of up to 80 D, and this is why a conservative jet tube length of 100 D was chosen for this study. After the jet exits the tube, it impinges onto a flat plate ($\oslash 200$ mm). Thereafter, the fluid is allowed to develop radially along the impinging plate, restricted only by a confining plate positioned at the nozzle exit. The water is then collected by a transparent reservoir tank positioned 200 mm above the pump in order to obviate cavitation and to prevent air bubbles entering the system. Finally, the water is returned to the pump, thus completing the flow circuit. A TSI PIV system was used to: visualise the flow field; extract velocity data from the jet flows; and study the effect of stagnation zone fluid dynamics on the nozzle exit velocity profile.

The PIV parameters in this study were chosen to give the clearest velocity vector plots with the lowest uncertainties. This was achieved by matching the image capture rate and interrogation area to capture the dynamics of the flow. Generally, there are five parameters that can be varied to optimise the PIV results: laser sheet thickness; particle size and concentration; interrogation area size; distance between each pixel, which is affected by the image magnification and camera resolution; and the distance travelled by each particle, which is affected by the time interval between each laser pulse. Table 1 shows the parameters used in this experimentation for each of the flow visualisation experiments carried out.

The experimentation apparatus was set up as shown in Fig. 2. The laser was orientated to dissect the jet, and the camera was orthogonally aligned and focused on the area of interest. The apparatus was filled with the working fluid to the water level shown in Fig. 2. This level was chosen to reduce the effects of ambient pressure on the flow structures formed. PIV tracer particles (silver-coated hollow glass spheres) were added until a sufficient concentration was met, as quantified by Riethmuller (2003). The tank was stirred until a homogeneous mixture of fluid to tracer particles was achieved within the system. The flow rate in the system was adjusted by changing the voltage applied to the centrifugal pump. The flow rate recorded from the rotameter and the water properties—dictated by the temperature recorded in the tank—were used to calculate the Re number. One thousand image pairs were recorded for each of the Re tested, and three thousand four hundred image pairs were recorded for the Reynolds stress analysis. Both the fluid dynamics surrounding the stagnation zone and their influence along the jet tube were assessed over a range of Reynolds numbers between $1350 < Re < 17{,}300$ and for H/D ratios between $0.25 < H/D < 8.75$. Generally, in jet analysis, Reynolds number is referenced to the jet's inner diameter (D) and the mean inlet velocity across the nozzle (V_m):
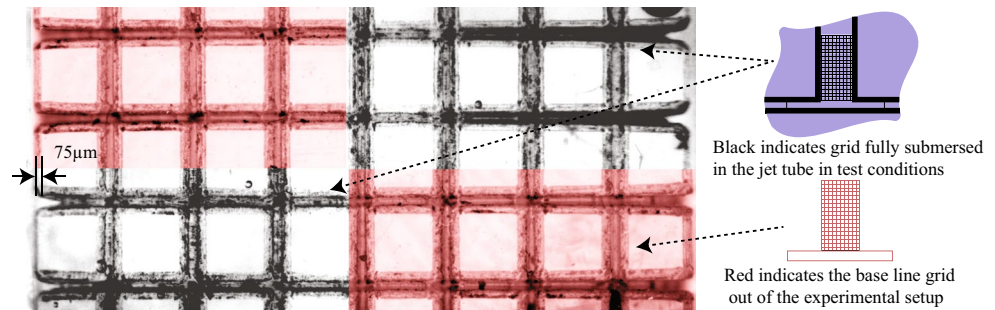
$$Re = \frac{\rho V_m D}{\mu} \tag{1}$$

where ρ and μ are density and dynamic viscosity, respectively. Velocity magnitude plots in this study are normalised to the mean inlet velocity of the jet (V_m) (Riethmuller 2003; Webb and Ma 1995). The Reynolds stress analysis presented in this paper was calculated in the streamwise direction using Eq. 2 and in the radial direction using Eq. 3.

$$\frac{\overline{u'u'}}{V_m^2} = \frac{\overline{u.u} - \bar{u}.\bar{u}}{V_m^2} \tag{2}$$

$$\frac{\overline{v'v'}}{V_m^2} = \frac{\overline{v.v} - \bar{v}.\bar{v}}{V_m^2} \tag{3}$$

where u and v are the PIV velocity components in the streamwise and radial direction, respectively.

Fig. 3 Grid to assess the influence of the slight refractive index mismatch between the tube and water

Black indicates grid fully submersed in the jet tube in test conditions

Red indicates the base line grid out of the experimental setup

2.1.1 Experimental uncertainty

The uncertainties in the primary measurements were minimised as follows: flow rate uncertainty was minimised with the utilisation of two calibrated rotameters, which were capable of recording flow rates between the range of: 1.6–18 l/min with a maximum uncertainty of 12 % and 0.2–2 l/min with a maximum uncertainty of 15 %.

The influence of image distortion in the jet tube was assessed and presented in Fig. 3. A small grid was laser cut out of acrylic and parameterised using a Keyence VHX digital microscope. This grid was then pictured in two locations: the first was the water-filled jet tube with its water jacket around it, as shown in Fig. 2, and the second was on its own in air. The distortion caused by the refractive index mismatch of water (1.33) against the acrylic jet tube (1.49) is shown in Fig. 3. There is little distortion across the jet tube with the maximum seen at the edges where distortions of up to 75 μm were observed. The authors believe that this difference is minimal and has not been corrected for throughout the paper; however, it may contribute to some uncertainty near the walls of the jet tube. In order to minimise the uncertainty with the rest of the PIV measurements, the following six rules developed by Keane and Adrian (1990) and TSI (1999) were strictly adhered to.

- One thousand particle image pairs, per interrogation area, were used in order to minimise the uncertainty in the statistical calculations for velocity magnitude. Three thousand four hundred image pairs were recorded to minimise the uncertainty in the Reynolds stress data.
- The interrogation area was chosen of sufficient size so that one vector reliably described the flow.
- In-plane displacements >25 % of the interrogation size were avoided.
- In-plane displacements <2 particle image diameters were avoided.
- Out-of-plane displacements >25 % of the laser sheet thickness were avoided.
- The camera exposure and laser intensity were balanced and clearly showed the particles in the image.

Multiple image pairs were fully processed in Insight 4G software, and the parameters varied until the above six rules were met and the system was aligned and focused. The images were divided into 40 × 40 interrogation regions that were interpolated down to a grid size of 24 × 24 with a deformation grid engine, and then 2D cross-correlation was performed, as presented by Scarano (2002). The resultant grid is shown in Fig. 7 and compared to the numerical grid. A square interrogation region was chosen because in jet impingement strong velocity components exist in both the streamwise u and the radial v directions. Displacement in the resultant cross-correlation map was measured with subpixel accuracy through Gaussian peak detection. Figure 4a shows a synthetic image that was used to compile two Gaussian noise maps to assess the accuracy of the PIV processing settings. The black regions of Fig. 4a are set to zero displacement, while the white region is set to 5 pixel displacement. This represents the average particle displacement of the PIV experimental results, and a transition occurs between the white and black sections. These artificially generated PIV images were imported into Insight 4G to assess the accuracy of the processing settings, and the resultant vector map is shown in Fig. 4b. Figure 4c plots the processed image with a blue colour band located between 4.95 and 5.05, and this represents a 2 % uncertainty. Although some noise exists, it is below a maximum uncertainty of 8 %. Figure 4d plots the profile extracted from the measurement plane in Fig. 4c and compares to the fully synthetic profile. This plot shows a maximum divergence from the fully synthetic plot of 6 %. These results show that an uncertainty of no more than 8 % is incurred as a result of the processing parameters used in this study.

The quantity of image pairs used for PIV in this study was assessed using a full-field analysis originally presented by Stafford et al. (2012), as shown in Fig. 5. As the sampling rate constitutes random sampling, standard error estimates were used to determine the uncertainty in the ensemble average velocity magnitude compared to a time-average flow field. The sample size of 1000 resulted in 98.5 % of the measurement region having <5 % error compared to the fully converged case. Therefore, 1000 image pairs are deemed to be a sufficient sampling quantity to accurately

Fig. 4 Assessing the PIV settings with synthetic and semisynthetic images
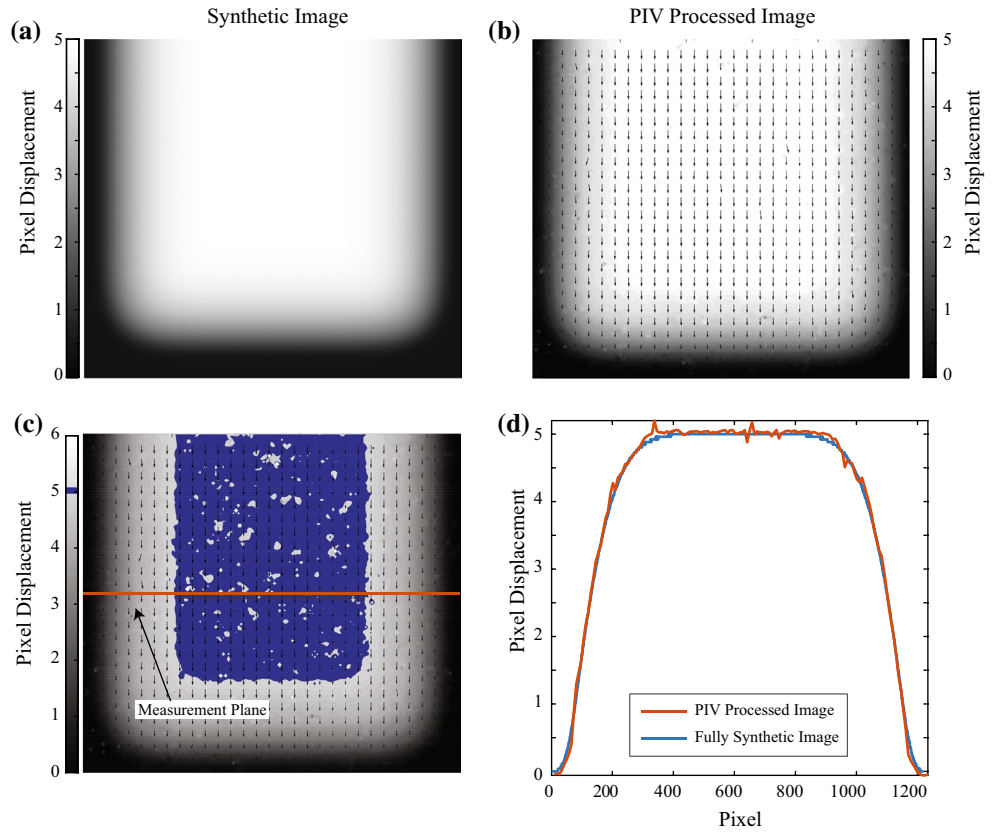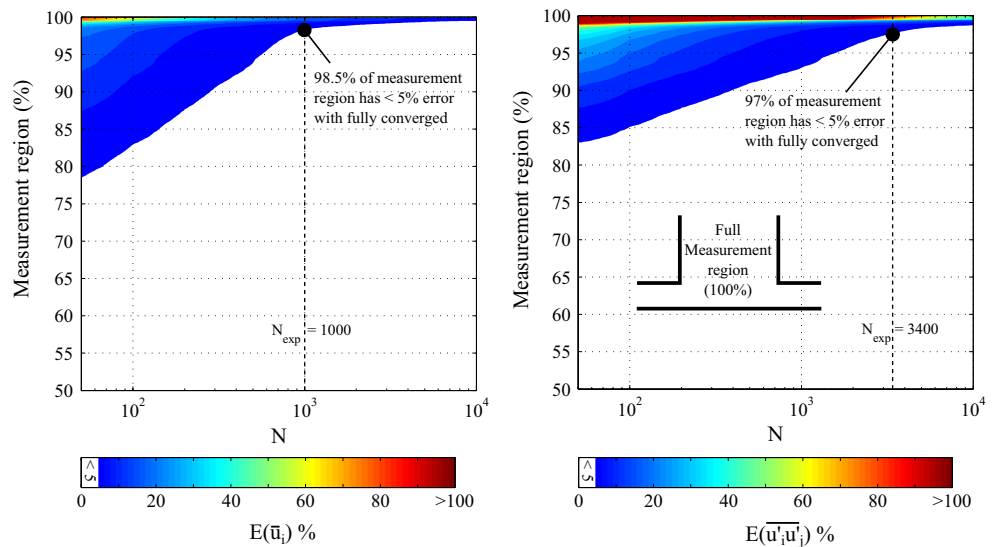

Fig. 5 Full-field analysis of the PIV results to determine the error resulting from sampling quantity

represent the velocity flow fields presented in this study. However, a greater number of images were required to accurately represent the time-average Reynolds stresses from the ensemble of measurements recorded. In total, 3400 images resulted in 97 % of the measurement region having <5 % error compared to the fully converged Reynolds stress.

Finally, in order to further validate the experimental setup, the volumetric flow rate was calculated at the nozzle exit from the 1000 averaged PIV vector plots and compared to the values recorded by the rotameter. These results showed a maximum divergence of <8 %. However, some of this variance is attributed to the uncertainty associated with the rotameter. Figure 6 plots the nozz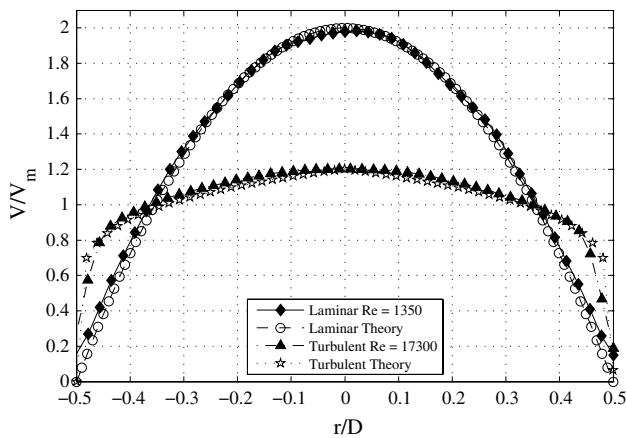le exit profiles for a jet confined to $H/D = 8.75$. The results are subsequently compared to theoretical fully developed nozzle exit profiles found in the literature. The fully developed theoretical

Fig. 6 Nozzle exit profiles extracted from the experimental results and compared to theoretical

laminar profile is shown in Eq. 4, which was taken from Bejan (2004a). The fully developed theoretical turbulent profile was taken from Fox et al. (2004b); however, this profile is for $Re > 20,000$ and is compared to a profile at $Re = 17,300$ as shown in Fig. 6. This turbulent profile was calculated using Eqs. 5 and 6, respectively.

$$\frac{v}{V_{\max}} = 2\left(1 - \left(\frac{r}{R}\right)^2\right); \tag{4}$$

$$\frac{v}{V_{\max}} = \left(1 - \frac{r}{R}\right)^{1/n}; \tag{5}$$

$$n = (-1.7 + 1.8 \log Re) \tag{6}$$

where $V_{\max}$ is the maximum velocity, R is the nozzle radius, and v is the local velocity. Both the experimental and the theoretical profiles converge upon each other with a maximum deviation of only 2 % between $-0.45 < r/D < 0.45$. This graph demonstrates the accuracy of the PIV results presented in this study having a maximum uncertainty of 8 %.

2.2 Numerical analysis

A numerical analysis was considered for a single turbulent flow case that was examined experimentally. This was the maximum Reynolds number ($Re = 17,300$) and lowest nozzle to impingement plate distance $H/D = 0.25$, respectively. The primary aim of the numerical analysis was to examine the boundary condition parameters L/D and nozzle exit velocity profile on predictive accuracy. This analysis is used to provide recommendations for the numerical analysis of low H/D impinging jets.

A steady three-dimensional RANS approach was utilised for the numerical analysis. A solution to the

governing equations of mass and momentum was achieved using the $k - \omega$ shear stress transport (SST) model (Menter 1994). A second-order scheme was implemented for discretisation, and the analysis was performed using a double precision solver in ANSYS Fluent (2011). The standard and additional SST closure constants used for this approach remained as defined in Fluent (2011). This model was selected based on the findings of previous studies in the literature on jet impingement (Zuckerman and Lior 2007, 2011). Zuckerman and Lior (2007) determined the most reliable numerical models that use the RANS approach for accurately predicting flow and heat transfer characteristics of impinging jets were the $k - \omega$ SST and $v^2 f$ models. A numerical model that replicated the experimental set-up described in Fig. 2 was used to validate the numerical approach with the current experimental data as a benchmark. A velocity boundary condition was prescribed at the tube inlet. A pressure outlet boundary condition was defined at the exit of the computational domain, located 12.5 D from the nozzle exit to reflect the experimental configuration in Fig. 2. The Boussinesq approximation is used to determine the Reynolds stresses presented from the numerical investigation, describing the relationship between turbulence stresses and mean strain rate (Zuckerman and Lior 2011). Using the strain rate tensor, $S_{ij} = 1/2[(\delta \overline{u}_i / \delta x_j) + (\delta \overline{u}_j / \delta x_i)]$, turbulent viscosity ($\mu_t$), and turbulent kinetic energy (k) predictions, the Reynolds stress tensor is formulated.

$$-\rho \overline{u_i' u_j'} = 2\mu_t \left(S_{ij} - \frac{1}{2} S_{kk} \delta_{ij}\right) - \frac{2}{3} \rho k \delta_{ij}. \tag{7}$$

2.2.1 Numerical uncertainty

In all simulations, a velocity was defined at the inlet, an ambient pressure was defined at the outlet, and a no-slip condition was set at the wall surfaces bounding the flow (impingement plate; confinement plate; inlet tube). The geometries were meshed using unstructured hexahedral cells, and near-wall refinement was achieved with $y^+ < 1$. A grid independence study was conducted to ensure results were insensitive to grid size (y^+ and global cell size). The final meshing parameters were selected to provide a trade-off between sufficient accuracy and limiting the demand on computational resources. The results of the mesh sensitivity study are listed in Table 2. Maximum local differences in the nozzle exit velocity profile for each grid over the largest grid size (mesh 5) are provided in Table 2. Five different grids were solved, spanning a tenfold increase in node count. Using this information, mesh 3 was chosen as the most appropriate grid to solve the numerical simulations. A centrally located 2D slice of the three-dimensional mesh, illustrating the grid, is presented in Fig. 7.

Table 2 Grid independence analysis on L/ D = 100 model

Mesh	Grid size (nodes)	Maximum local difference (%) nozzle exit velocity profile
1	1.63×10^6	13.19
2	2.6×10^6	2.81
3	4.75×10^6	1.32
4	8.77×10^6	0.3
5	16.22×10^6	–

**Fig. 7** The grids used for the PIV experimentation and the numerical solution
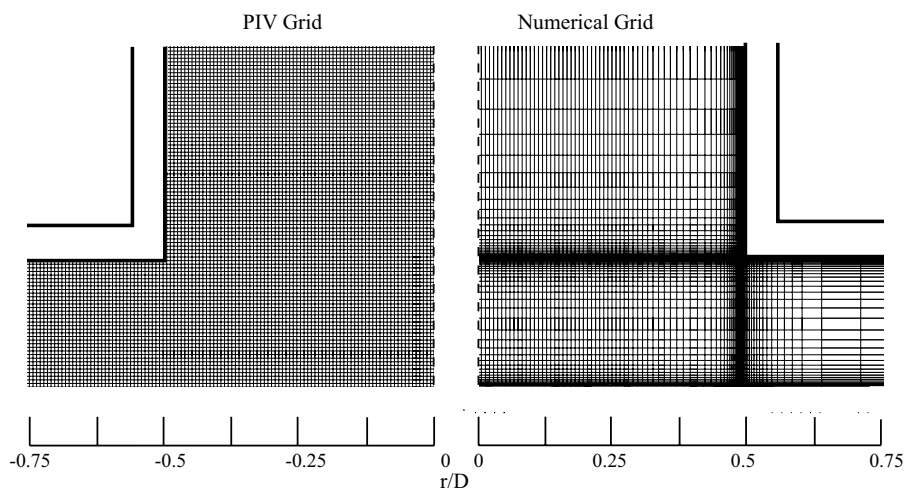
3 Results and discussion

This section compares and discusses results found both experimentally and numerically to fully assess the influence that the stagnation zone has on the fluid dynamics at the nozzle exit of an impinging jet at low *H/D* ratios. Flow characteristics around the nozzle exit of a classical normally impinging, submerged, and confined liquid jet are presented. The experimental apparatus and numerical set-up discussed earlier were used to measure and predict full-field velocity magnitude plots. These plots are then used to illustrate the effect of the stagnation zone fluid mechanics on the jet's nozzle exit velocity profile.

A comparison between the numerically predicted and experimentally measured full-field velocity profiles at the nozzle exit is presented in Fig. 8a. Both the experimentally measured and numerically predicted results are axisymmetric about the jet centre; therefore, the plots presented in Fig. 8a represent the complete jet impingement. Figure 8a shows the experimentally measured PIV time-averaged velocity magnitude plot of a turbulent impinging jet confined to a $H/D = 0.25$ at a $Re = 17{,}300$. The velocity magnitudes in every plot presented in this paper are normalised using the mean axial velocity across the nozzle exit (V_m). Figure 8a also shows the numerical prediction of the

experimental configuration. The numerical and experimental results both show that the decelerating axial velocity in the stagnation zone influences the nozzle exit velocity profile. This deceleration in axial velocity is caused by the backpressure from the jet's impingement. This stagnation zone backpressure effect also influences the velocity profiles in the tube itself. Figure 8a shows a steady decrease in velocity along the centre-line of the jet as it approaches the impingement surface for both the numerical and experimental results. This decrease in centre-line velocity results in an increase in velocity around the periphery of the jet to conserve mass flow $(\rho V_m \pi D^2)/4$. As a result, the centre-line velocity at the nozzle exit is lower than towards the periphery. This nozzle exit velocity profile is unique for low *H/D* ratios and neither resembles fully developed nor undeveloped exit flow profiles. It is evident from Fig. 8a that a combination of both physical constraints and fluidic backpressure effects defines the shape of the nozzle exit velocity profile. The numerical and experimental results show good agreement as shown in the % difference plot, presented in Fig. 8b. The majority of the velocity magnitude numerical results are within 7 % of those experimentally measured as indicated by the grey regions in Fig. 8b. The biggest differences occur along the jet tube wall. In this near-wall region, it is difficult to record quantitate

Fig. 8 Turbulent jet impingement and jet tube plots at $H/D = 0.25$ and $Re = 17,300$ **a** Full-field normalised velocity magnitude plots of experimentally measured and numerically predicted. **b** Plots the % difference between the experimentally measured and numerically predicted results
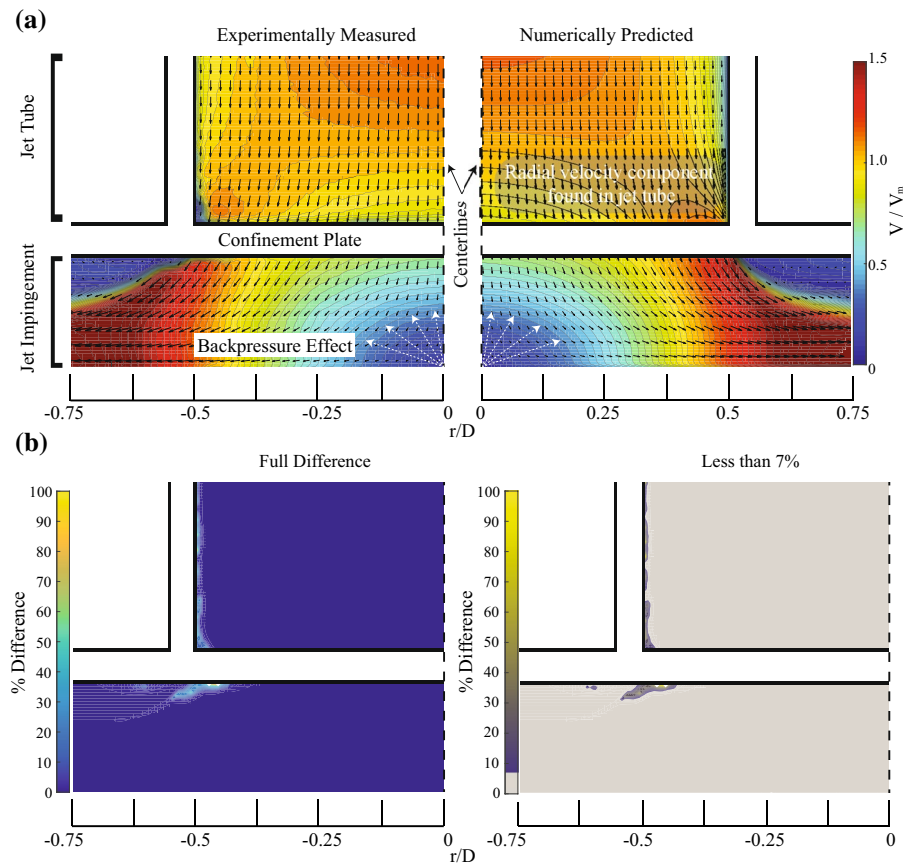

experimental data using the PIV technique because of the flaring that occurs where the laser enters and exits the jet tube. There is also a difference of $\approx 15-20\,\%$ at the onset of the shear layer in the impingement region of the jet, and this difference could be caused by the limitations of the RANS numerical prediction or experimental error at the near-wall region of the jet tube and the confining surface. Overall, the agreement is sufficient to validate the numerical model, as the difference is minor and within the same order of magnitude as the uncertainty in experimental measurement.

Figure 8 shows that for low H/D, the influence of the stagnation zone backpressure becomes prominent and influences the shape of the nozzle exit velocity field. Figure 9 plots the numerically predicted pressure field found in an impinging jet confined to a $H/D = 0.25$ and a $Re = 17,300$. This plot clearly shows the backpressure effect, where the jet pressure at the centre-line gradually increases between $y/D = 0.75$ and $y/D = 0$. The jet tube velocity profiles remain unaffected by the backpressure for $y/D > 0.75$, as shown in Fig. 9e, f. However, the velocity profiles are clearly affected by the impingement backpressure for $y/D < 0.75$, as shown in Fig. 9a–d. It is currently challenging to accurately measure full-field pressure experimentally. However, given the agreement with velocity field

data presented in this study, it is likely that they show similar trends to the numerical prediction presented in Fig 9.

A comparison between the numerical and the experimental results for Reynolds stress is shown in Fig. 10. Figure 10a presents Reynolds stress in the radial (u) direction, with the numerical results showing similar trends to the experimental however with substantially different magnitudes in the shear layer regions. Reynolds stress measurements and predictions in the streamwise (v) direction are qualitatively similar, but also show quantitative differences in the shear layer region as shown in Fig. 10b. These differences highlight the limitations of the RANS approach for modelling low H/D jet impingement. Another indication of the differences between measured and predicted turbulence statistics is presented in Fig. 10c. This has been produced by extracting Reynolds stress along a measurement line at a $y/D = 0.125$. Wall-normal stresses are higher than wall-parallel stresses directly beneath the jet and up to $|\,r/D\,| = 0.6$. However, as the fluid is forced to turn in the radial direction, a crossover is both experimentally measured and numerically predicted. The measurement line intersects the shear layer, where wall-parallel stresses increase by an order of magnitude compared to that beneath the jet exit. The numerical results underpredict the Reynolds stresses seen in the shear layer immediately

Fig. 9 Numerically predicted pressure field and normalised velocity profiles (**a**–**f**) at various *y*/*D* within the tube to illustrate the back pressure phenomenon at $H/D = 0.25$ and $Re = 17,300$
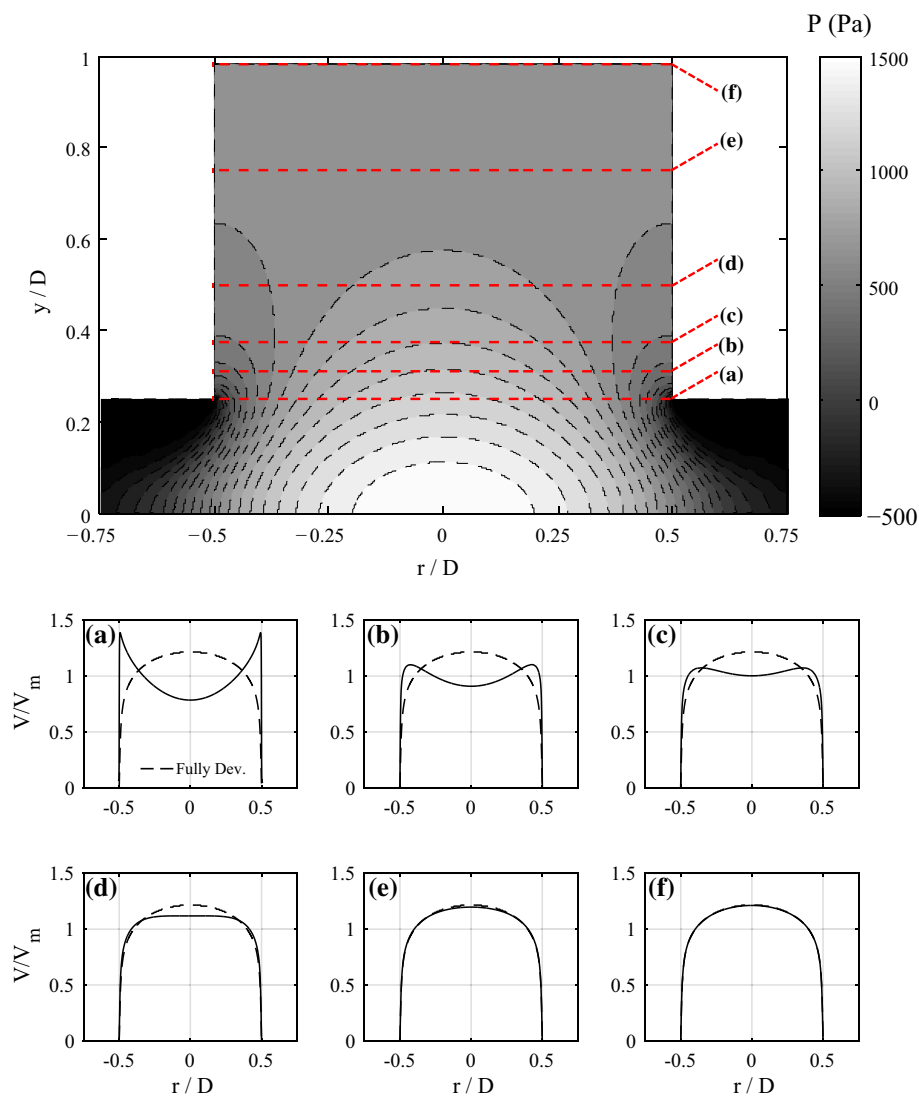

at the nozzle exit (by as much as twofold). Two underlying assumptions when approximating turbulent effects with two-equation models are low importance of pressure gradients and the negligible anisotropy of turbulence, or Reynolds stresses (Zuckerman and Lior 2011). In the current low *H*/*D* arrangement, a sharp change in fluid direction immediately at the nozzle exit is required. Coupled with the stagnation region backpressure extending upstream into the nozzle, the pressure gradients are significant and the former modelling assumption may be limited. Similarly, the latter assumption of isotropy has been shown to have limited applicability for stagnation regions (Zuckerman and Lior 2011). The hybrid SST scheme employed in this study combines the strengths of the $k - \omega$ model near the wall with the $k - \epsilon$ model away from the wall. One reason this hybrid scheme has been successful previously is due to the $k - \epsilon$ model producing reasonable predictions in the free jet region (Dewan et al. 2012). However, for the current

investigation at low *H*/*D*, the conventional free jet zone (illustrated in Fig. 1) is effectively removed by the stagnation zone backpressure. This finding suggests that either alterations to the closure equations/coefficients for this flow configuration or higher fidelity approaches may be necessary to accurately quantify the turbulent statistics of jets at this level of confinement.

Figure 11 illustrates the effect of different confinement heights on the nozzle exit velocity profiles of a turbulent submerged and confined impinging jet at $Re = 17,300$. As the confinement height is reduced from $H/D = 1$, the jet's centre-line velocity decreases, while the velocity at the edge of the nozzle increases. As a result, the profile across the nozzle confined to a $H/D = 0.25$ has a peak velocity at the edge which decays to a trough at the centre-line of the jet, $r/D = 0$. The centre-line velocity ($r/D = 0$) is approximately 35 % lower than the peak velocity for a nozzle confined to a $H/D = 0.25$. The fluidic mechanism responsible

Fig. 10 Experimental and numerical full-field Reynolds stress plots for an impinging jet confined to a $H/D = 0.25$ and $Re = 17{,}300$: **a** Plots the full-field radial u direction Reynolds stress $\overline{u'u'}/V_m^2$; **b** plots the full-field streamwise v direction Reynolds stress $\overline{v'v'}/V_m^2$; and **c** plots the wall-normal and wall-parallel Reynolds stresses across the measurement plane taken at $y/D = 0.125$
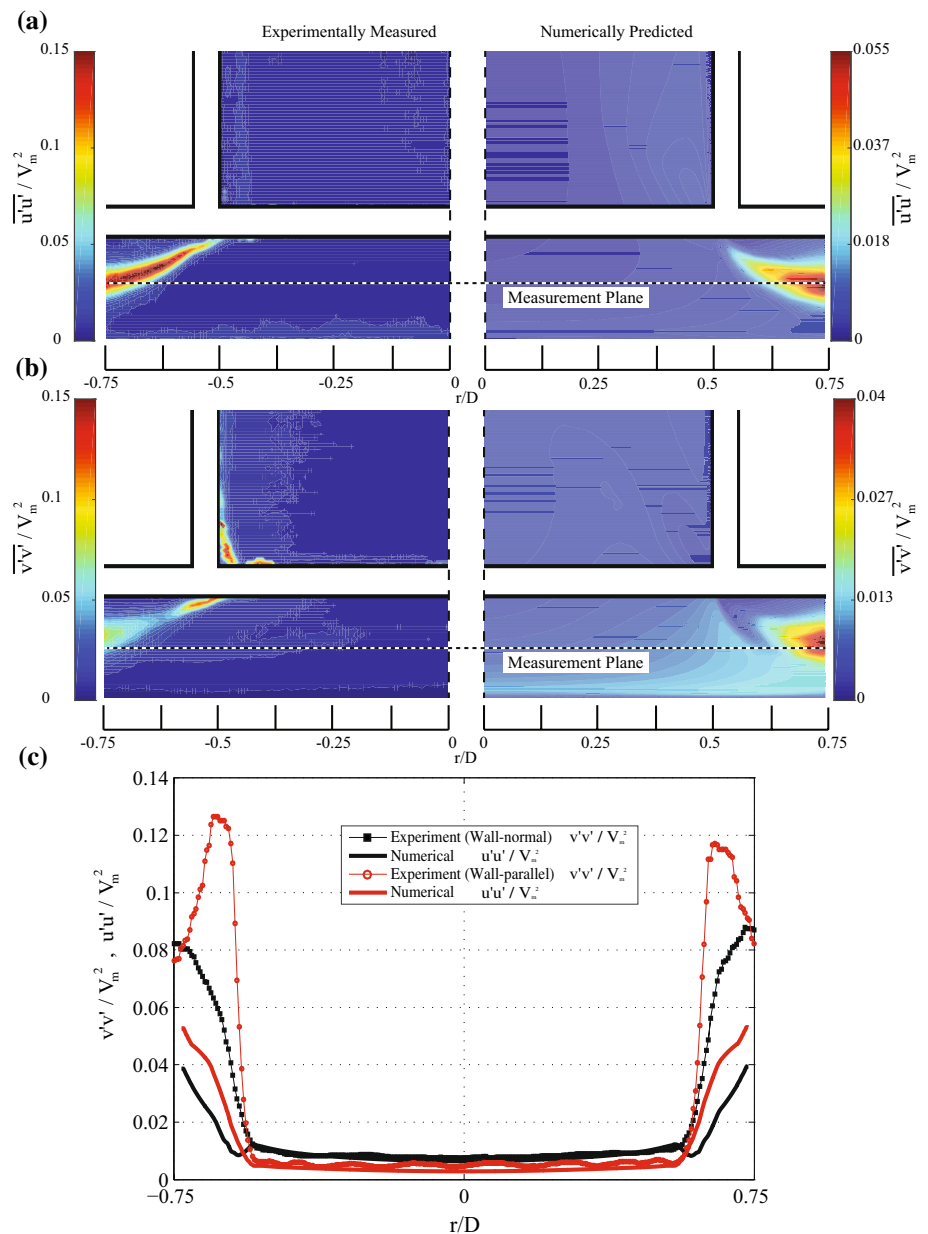
for the shape of the nozzle exit profile is the backpressure caused by the impingement in the stagnation zone. This backpressure region partially impedes the jet's centre-line flow, which results in an increase in velocity at the edge of the nozzle exit, as shown in Fig. 11. For confinements $H/D < 1$, the profile resembles neither a fully developed nor developing nozzle flow, and therefore to use either of these profiles as an initial boundary condition at the nozzle exit in a numerical model would result in errors.

Figure 12 illustrates the influence of Reynolds number on the velocity profiles across the nozzle exit for a confinement at $H/D = 0.25$. The profiles between $3400 < Re < 17{,}300$ conform together relatively well, with a maximum divergence across the nozzle exit of ∼11 %. This shows that the

normalised velocity profile between $3400 < Re < 17{,}300$ is largely independent of Reynolds number. The experimental results plotted in this study also show that for different H/D spacing, the normalised turbulent velocity profiles are independent of Re number. However, the velocity at $Re = 1350$ exhibits a different profile as it is within the laminar regime. As a result, it is assumed that the only effect that a change in Reynolds number has on the normalised nozzle exit velocity profile is when the flow condition changes from laminar to turbulent regimes. As the nozzle exit velocity profiles are relatively insensitive to changes in Reynolds number, the numerical parametric study on the influence of nozzle boundary condition was conducted for a fixed $Re = 17{,}300$ and also the lowest confinement height $H/D = 0.25$.
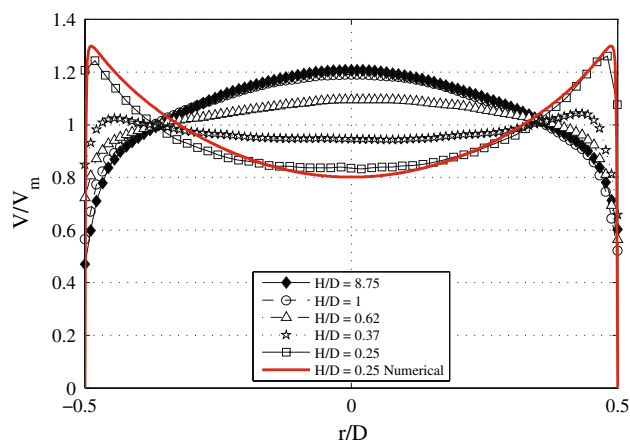
Fig. 11 Experimentally measured nozzle exit velocity profiles for a turbulent jet exiting at $Re = 17,300$ showing the effect of different H/D confinement ratios between $0.25 < H/D < 8.75$, also plotted is a numerically modelled nozzle exit profile at confinement of $H/D = 0.25$
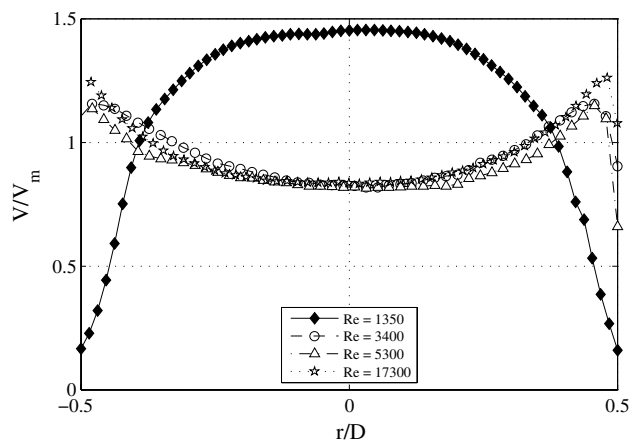

Fig. 12 Experimentally measured nozzle exit velocity profiles depicting the influence of Reynolds number for a confinement of $H/D = 0.25$

Figure 11 plots the nozzle exit profiles with these constraints for both experimental and numerical results. They conform to within 4 % of each other, thus further validating this numerical model.

Figure 13 shows the numerically predicted velocity magnitude plots for a range of initial boundary conditions. In order to save on computational time, simplified impinging jet models are used with predefined nozzle exit profiles. For low H/D confinements, this study shows that in reality the nozzle exit velocity profile is different in the conventionally used fully developed or developing boundary conditions found in the literature (Hattori and Nagano 2004; Behnia et al. 1999; Satake and Kunugi 1998; Thielen et al. 2005). It is therefore important to examine the influence

that an incorrectly defined nozzle exit boundary condition has on the surrounding fluid dynamics. Figure 13a shows a numerically predicted stagnation zone that results from a predefined flat or developing velocity profile set 100 D from the nozzle exit. This model was computationally demanding as the velocity profile within the entire 100 D jet tube was solved. While the tube length is conservative considering development in turbulent pipe flow (Bejan 2004c), it reflects the experimental arrangement in Fig. 2. The influence of inputting a predefined velocity condition at the nozzle exit is shown in Fig. 13 for (b) flat developing profile, (c) theoretical turbulent profile, and (d) nozzle exit profile comprising of axial and radial components extracted from the numerical results in Fig. 8a. The flat and turbulent inlet boundary conditions result in different velocity magnitudes and fluid dynamics within the stagnation zone of an impinging jet when compared to both the experimental and numerical results, shown in Fig. 8a and Fig. 13a, respectively. In particular, increased velocity gradients are evident at the impingement surface as the jet's flow is forced from an axial to radial direction. Figure 13d shows the resultant plot from an axial stagnation zone input profile with a radial component. This plot matches the full model in Fig. 13a. Figure 8a shows a radial velocity component in the jet tube that is required to fully capture the fluid mechanics at the nozzle exit. Incorrectly defined boundary conditions, such as those shown in Fig. 13b, c, will also affect wall flux statistics such as heat and mass transfer at the impingement surface, especially if augmentations are made to the impingement surface in order to enhance heat transfer.

Figure 14 presents the nozzle exit velocity profiles that result from predefined velocity boundary condition profiles set at different heights (L/D) from its nozzle exit. Two initial velocity profiles are assessed: a uniform initial flow profile, Fig. 14a; and a turbulent initial flow profile, Fig. 14b. Using a uniform profile boundary condition, a jet tube with $L/D > 12$ would need to be defined to produce a nozzle exit profile within 5 % of the validated $L/D = 100$ prediction. This is because the flow is still developing for $L/D < 12$. For example, if a uniform velocity boundary condition is set at $L/D = 1$, the resultant centre-line velocity profile at the nozzle exit ($r/D = 0$) is under predicted by ~17 % and the near-wall velocity ($r/D = 0.5$) is over predicted by ~15 %. Bejan (2004b) showed that in pipe flow, a fully developed turbulent condition is met after $L/D \sim 10$. The discrepancy between their findings and what is presented here is caused by the stagnation zone backpressure effectively increasing the jet tube length (L/D) necessary for a fully developed profile to exist. Figure 14b shows the influence of an initial turbulent flow profile set at different heights (L/D) on the nozzle exit profile. Again, if the desired nozzle exit profile were to be within 5 % of

Fig. 13 Numerically modelled results illustrating the velocity magnitude plots within the stagnation zone for an impinging jet at $Re = 17{,}300$ and $H/D = 0.25$; the predefined velocity profile boundary conditions are **a** flat velocity profile set 100 D from nozzle exit, **b** flat profile at the nozzle exit, **c** theoretical turbulent profile set at the nozzle exit, and **d** a stagnation zone profile with axial and radial components set at the nozzle exit
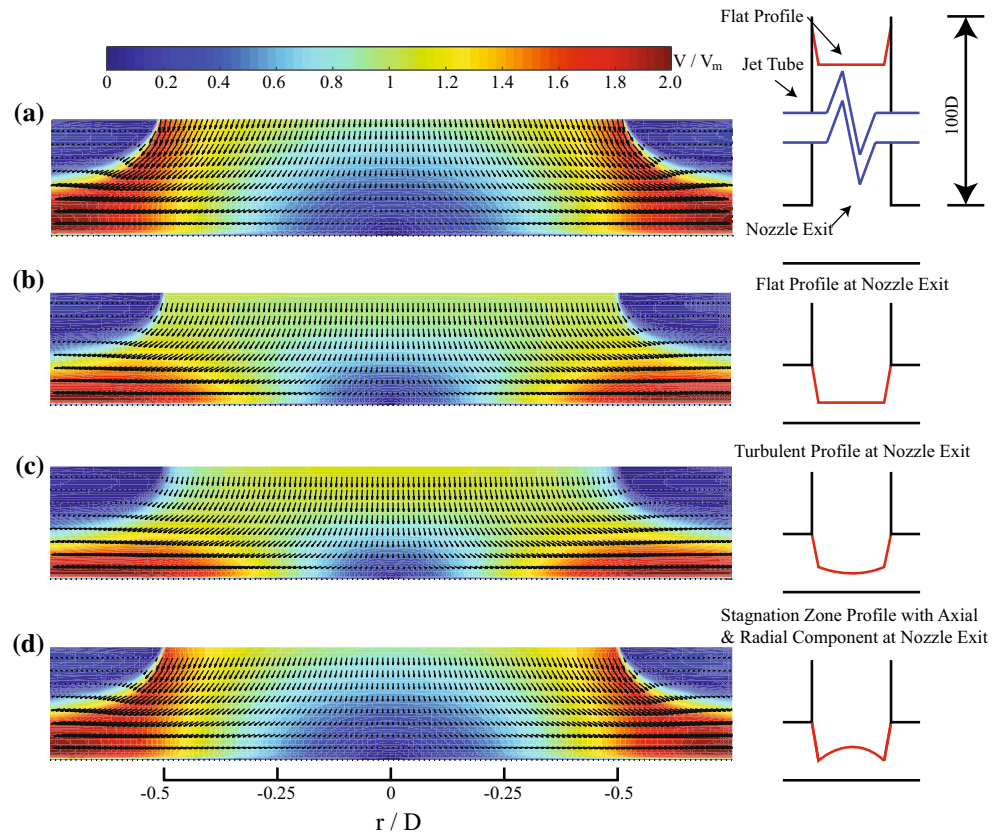
the validated prediction ($L/D = 100$), a jet tube with a length $L/D > 0.5$ would also need to be modelled. This decrease in required jet tube length (L/D) is expected, as the approaching flow no longer needs the additional development length required when imposing a uniform velocity boundary condition. Figure 14b also highlights significant differences when using $L/D < 0.5$. For $L/D = 0.25$, the centre-line velocity is over predicted by ~19 %. In this configuration, the stagnation zone backpressure is not captured sufficiently, and a falsely high centre-line velocity is imposed. From these results, it shows that if the model is to truly represent (within 5 %) a fully developed turbulent nozzle exit profile at low H/D, two actions are required: firstly, a jet tube length $L/D > 0.5$ is needed, and secondly, a theoretically turbulent velocity boundary condition is required at the inlet of this jet tube. Figure 14b also shows that for $L/D > 1$ the jet tube length (L/D) has little influence over the flow profile of the impinging turbulent jet.

The impact of inlet boundary condition on the nozzle exit velocity profile has been demonstrated. Variations in nozzle exit velocity can also affect predictions of transport phenomena at the impingement surface. Figure 15 plots the wall shear stress across the impingement surface for the experimental results compared to the numerical results with different boundary conditions. The radial slope in wall shear stress goes through a transition at $|r/D| \approx 0.3$,

a characteristic which is not evident in higher H/D scenarios Tu and Wood (1996). A low slope exists in the stagnation zone for $0 < |r/D| < 0.3$, while an increase in the radial slope occurs for $0.3 < |r/D| < 0.6$. This increase is produced by the modified nozzle exit flow. This modified profile, shown in Fig. 11, has maximal velocity at $0.4 < |r/D| < 0.5$. This imparts an increase in wall velocity gradient at the impingement surface downstream. Similar trends are seen between the numerical and experimental results; however, an ≈ 20 % numerical under prediction is seen at $|r/D| = 0.7$. The location of this difference also coincides with the under predictions in Reynolds stresses observed in Fig. 10. This suggests that the limitations of this two-equation RANS model in predicting turbulent stresses in the shear layer translate to differences at the impingement surface when these high stresses are in close proximity to the wall. The wall shear stress resulting from the mapped stagnation zone nozzle profile boundary condition closely matches the fully modelled jet tube base case; however, significant differences are shown between the base case and the uniform and fully developed nozzle inlet boundary conditions. In the impingement zone, directly beneath the nozzle exit ($-0.5 < r/D < 0.5$), the local wall shear stress τ_w varies by up to +100 % when using a uniform or fully developed initial nozzle flow profile compared to the experimental profile. It is probable that these
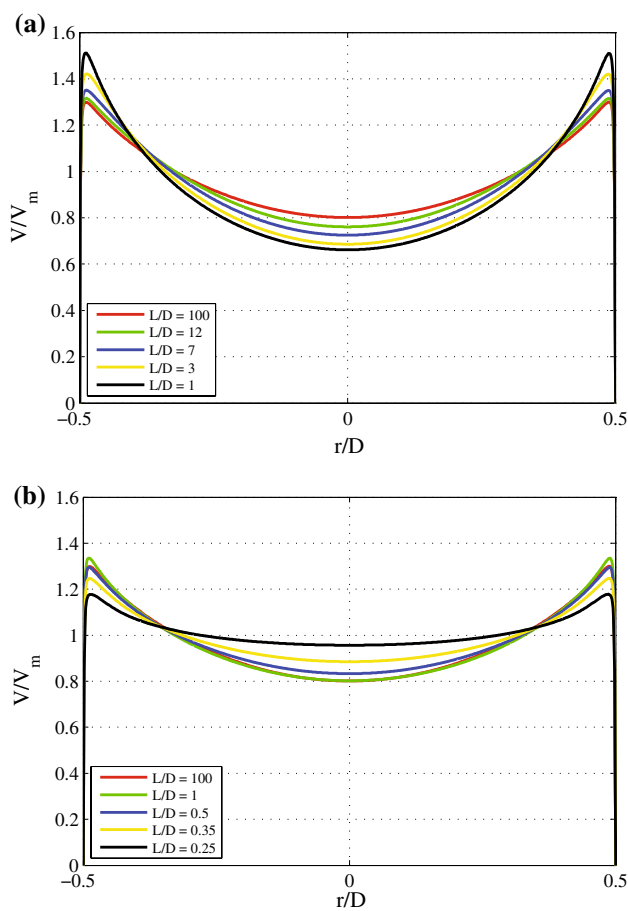
(a)

(b)

Fig. 14 Numerically modelled nozzle exit velocity profiles for predefined boundary condition velocity profiles set between $0.25 < L/D < 100$ using **a** a uniform profile and **b** a fully developed turbulent flow profile
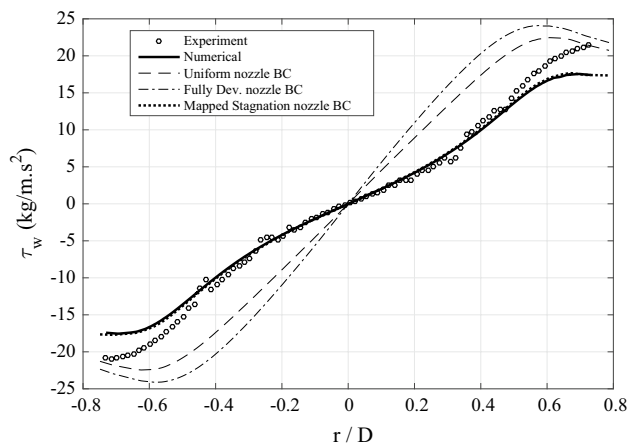

Fig. 15 The impact of numerical boundary condition on the wall shear stress across the jet impingement surface

significant differences will affect surface transport characteristics such as heat transfer.

The results found in this paper are of vital importance regarding the accurate modelling of impinging jets confined to low H/D ratios. It is self-evident that if the initial boundary conditions of numerical models are not defined correctly, it propagates into predictive uncertainty regardless of the model that is being implemented. Similarly, the results of this parametric study can be used to provide useful estimates of numerical uncertainty due to boundary condition assumptions in turbulent impinging jet studies. It is recommended that a theoretical turbulent velocity profile is inputted at the inlet of a jet tube with a length $L/D > 0.5$ when simulating a fully developed turbulent jet at low H/D spacing. This finding is important with regard to complex models addressing impingement surface augmentations or arrays of jets or both. Numerical analyses such as DNS will also indirectly benefit from this work, as there may not be a need to model the entire jet tube, which is computationally demanding.

4 Conclusions

This paper describes the nozzle exit velocity profiles for a classical normally impinging submerged and confined liquid jet. The velocity profiles used as boundary conditions within the computational fluid dynamic literature do not account properly for the stagnation zone backpressure effect. The objective of this paper is to present experimental and numerical results to illustrate the effect that the stagnation zone backpressure has on the nozzle exit velocity profile for low H/D ratios. The following conclusions are inferred:

– Within the stagnation zone of an impinging jet, the fluid's velocity is influenced by the target surface causing a deceleration in axial velocity constituting an impingement. The backpressure as a result of this impingement affects the nozzle exit velocity profile for $H/D < 1$.
– As the H/D ratio is reduced, the stagnation zone backpressure effect increases. For a turbulent jet issuing at $Re = 17,300$ and confined to a $H/D = 0.25$, the velocity profile across the nozzle exit shows a peak towards the edge followed by a trough with a 35 % drop in velocity towards the centre. The laminar jet's nozzle velocity profile is effectively compressed as H/D is reduced, and shows a 30 % reduction in centre-line velocity.
– Laminar and turbulent jets exhibit different nozzle exit velocity distributions even at low H/D, although their shape is still strongly influenced by the stagnation zone backpressure.

– The selection of a suitable inlet boundary condition is an important factor for capturing the stagnation zone backpressure and validating the suitability of numerical models with experimental data. The numerical results show that if the model is to represent a fully developed turbulent nozzle exit profile within a 5 % accuracy, the following two initial boundary conditions must be adhered to: (i) a jet tube length $L/D > 0.5$ and (ii) a theoretically turbulent velocity boundary condition at the inlet.

– An alteration in the radial slope of wall shear stress was observed and also attributed to the stagnation zone backpressure effect. Neglecting the impact of backpressure on the nozzle exit profile produces errors in the numerical predictions of over 100 % in local wall shear stress compared to the experimentally validated solution. This finding highlights the importance of adhering to the previous boundary condition rules when investigating low H/D configurations and surface transport processes.

This paper shows that the nozzle exit velocity profile is heavily influenced by the stagnation zone backpressure effect for low H/D constraints. The results from this study can be used to generate nozzle exit velocity profiles with greater accuracy for numerical simulations confined to similar conditions.

Compliance with ethical standards

Conflict of interest The authors declare that they have no conflict of interest.

References

Alimohammadi S, Murray DB, Persoons T (2014) Experimental validation of a computational fluid dynamics methodology for transitional flow heat transfer characteristics of a steady impinging jet. J Heat Transf 136:091703–091703 06

ANSYS (2011) Fluent User's Guide, Release 14.0. ANSYS Inc, Pennsylvania

Behnia M, Parneix S, Shabany Y, Durbin P (1999) Numerical study of turbulent heat transfer in confined and unconfined impinging jets. Int J Heat Fluid Flow 20(1):1–9

Bejan A (2004a) Convection heat transfer, chapter 3 (equation 3.22), 3rd edn. Wiley, New Jersey

Bejan A (2004b) Convection heat transfer, chapter 8 (equation 8.4), 3rd edn. Wiley, New Jersey

Bejan A (2004c) Convection heat transfer, 3rd edn. Wiley, New Jersey

Caggese O, Gnaegi G, Hannema G, Terzis A, Ott P (2013) Experimental and numerical investigation of a fully confined impingement round jet. Int J Heat Mass Transf 65:873–882

Deshpande MD, Vaishnav RN (1982) Submerged laminar jet impingement on a plane. J Fluid Mech 114:213–236 1

Dewan A, Dutta R, Srinivasan B (2012) Recent trends in computation of turbulent jet impingement heat transfer. Heat Transf Eng 33(4–5):447–460

Fitzgerald JA, Garimella SV (1998) A study of the flow field of a confined and submerged impinging jet. Int J Heat Mass Transf 41(8â9):1025–1034

Fox R, McDonald A, Pritchard P (2004a) Introduction to fluid mechanics, 6th edn. Wiley, New Jersey

Fox R, McDonald A, Pritchard P (2004b) Introduction to fluid mechanics. Chapter 8 (equation 8.22 and 8.33), 6th edn. Wiley, New Jersey

Gardon R, Akfirat J (1965) The role of turbulence in determining the heat-transfer characteristics of impinging jets. Int J Heat Mass Transf 8(10):1261–1272

Garimella SV, Rice RA (1995) Confined and submerged liquid jet impingement heat transfer. J Heat Transf 117:871–877 11

Hadziabdic M, Hanjalic K (2008) Vortical structures and heat transfer in a round impinging jet. J Fluid Mech 596:221–260 1

Hattori H, Nagano Y (2004) Direct numerical simulation of turbulent heat transfer in plane impinging jet. Int J Heat Fluid Flow 25(5):749–758

Jambunathan K, Lai E, Moss M, Button B (1992) A review of heat transfer data for single circular jet impingement. Int J Heat Fluid Flow 13(2):106–115

Jeffers N (2009) On the heat transfer and fluid mechanics of a normally-impinging, submerged and confined liquid jet. Ph.D. Thesis from the University of Limerick, Ireland

Keane RD, Adrian RJ (1990) Optimization of particle image velocimeters, part 1, double pulsed systems. Meas Sci Technol 1(11):1202–1215

Lienhard J (1995) Liquid jet impingement. Annu Rev Heat Transf 6:199–270

Martin H, James P, Thomas J, Irvine F (1977) Heat and mass transfer between impinging gas jets and solid surfaces. Adv Heat Transf 13:1–60

Menter FR (1994) Two-equation eddy-viscosity turbulence models for engineering applications. AIAA J 32:1598–1605

Polat S, Huang B, Mujumdar S, Douglas W (1989) Numerical flow and heat transfer under impinging jets: a review. Annu Rev Numer Fluid Mech Heat Transf 2:157–197

Riethmuller M (2003) Particle image velocimetry. vonKarman Institute for Fluid Dynamics -Lecture Series

Satake S, Kunugi T (1998) Direct numerical simulation of an impinging jet into parallel disks. Int J Numer Methods Heat Fluid Flow 8(7):768–780

Scarano F (2002) Iterative image deformation methods in piv. Meas Sci Technol 13:1–19

Stafford J, Walsh E, Egan V (2012) A statistical analysis for time-averaged turbulent and fluctuating flow fields using particle image velocimetry. Flow Meas Instrum 26:1–9

Thielen L, Hanjalic K, Jonker H, Manceau R (2005) Predictions of flow and heat transfer in multiple impinging jets with an elliptic-blending second-moment closure. Int J Heat Mass Transf 48(8):1583–1598

TSI (1999) Particle image velocimetry (piv): theory of operation, 2nd edn. TSI Inc, Minnesota

Tu C, Wood D (1996) Wall pressure and shear stress measurements beneath an impinging jet. Exp Therm Fluid Sci 13(4):364–373

Webb B, Ma C (1995) Single-phase liquid jet impingement heat transfer. Adv Heat Transf 26:105–217

Zuckerman N, Lior N (2007) Radial slot jet impingement flow and heat transfer on a cylindrical target. J Thermophys Heat Transf 21:3

Zuckerman N, Lior N (2011) Jet impingement heat transfer: physics, correlations, and numerical modeling. Adv Heat Transf 39:565–631